

**MEASUREMENT OF HELICITY PARAMETERS IN TOP QUARK DECAY**Charles A. Nelson<sup>1</sup> and Andrew M. Cohen*Department of Physics, State University of New York at Binghamton**Binghamton, N.Y. 13902-6016***Abstract**

The standard model(SM) predicts only a  $g_{V-A}$  coupling in  $t \rightarrow W^+b$  decay. However, if additional Lorentz structures exist, they can manifest themselves in high energy processes such as this via non-SM values of the helicity parameters describing  $t \rightarrow W^+b$ . Plots and tables of the values of these helicity parameters are obtained for various coupling strengths. Three phase-type ambiguities are uncovered:  $g_{V-A} + g_{S+P}$  with effective-mass scale  $\Lambda_{S+P} \sim -35\text{GeV}$ ,  $g_{V-A} + g_{f_M+f_E}$  with  $\Lambda_{f_M+f_E} \sim 53\text{GeV}$ , and an arbitrary sign-flip in the  $b_L$  amplitudes  $A_X(\lambda_b = -1/2) = -A_{V-A}(\lambda_b = -1/2)$ . These ambiguities are analyzed so that they might be partially resolved when experiments resume at the Fermilab Tevatron.

---

<sup>1</sup>Electronic address: cnelson @ bingymb.cc.binghamton.edu

# 1 Helicity Amplitudes and $\alpha, \beta, \gamma$ Relative Phases

For  $t \rightarrow W^+b$  decay, the four on-shell helicity amplitudes  $A(\lambda_{W^+}, \lambda_b)$  can be uniquely determined by measurement of four moduli and three relative phases. In Fig. 1, measurements in the right and left columns are respectively of order  $\mathcal{O}(L^2)$  and  $\mathcal{O}(R^2)$ . The interference measurements between the two columns are of order  $\mathcal{O}(LR)$ .  $L$  and  $R$  denote the  $b$  quark's helicity  $\lambda_b = \mp 1/2$ . The values of  $A(\lambda_{W^+}, \lambda_b)$  for the standard model(SM) are given in the top row of Table 1. For the pure  $V - A$  coupling of the standard model, the left-handed helicity  $\lambda_b = -1/2$  amplitudes dominate by 1 to 2 orders of magnitude for  $m_b \sim 4.5\text{GeV}$ . Intrinsic and relative signs of these helicity amplitudes are determined by the Jacob-Wick phase convention.

The layout of the corners in Fig. 1 has been chosen to reflect the layout in the following probability plots for  $P(W_L)$  versus  $P(b_L)$  where

$$P(W_L) = \text{Probability } W^+ \text{ is longitudinally polarized, } \lambda_{W^+} = 0$$

$$P(b_L) = \text{Probability } b \text{ is left-handed, } \lambda_b = -1/2$$

The focus of this paper is on direct measurements of these  $b_L$  amplitudes by forthcoming experiments at the Fermilab Tevatron[1] and at the CERN LHC[2] relative to the anticipated pure  $V - A$  predictions. If, for instance, sizable  $b_R$  amplitudes were found to occur by these experiments, further analysis of coupling and phase-type ambiguities may be warranted. Likewise, when more precise measurements become possible in later experiments at the LHC or near the  $t\bar{t}$  threshold at a linear  $e\bar{e}$  collider, higher order QCD and EW corrections must be included, see [3].

Plots and tables of the values of the helicity parameters are given in terms of a “ $(V - A) +$  additional Lorentz structure”. Generically, we denote these additional couplings by

$$g_{Total} \equiv g_L + g_X \tag{1}$$

$$X = \begin{cases} X_c = \text{chiral} = \{V + A, S \pm P, f_M \pm f_E\} \\ X_{nc} = \text{non-chiral} = \{V, A, S, P, f_M, f_E\}. \end{cases}$$

For  $t \rightarrow W^+b$ , the most general Lorentz coupling[4] is  $W_\mu^* J_{bt}^\mu = W_\mu^* \bar{u}_b(p) \Gamma^\mu u_t(k)$  where  $k_t = q_W + p_b$ , and

$$\begin{aligned} \Gamma_V^\mu = & g_V \gamma^\mu + \frac{f_M}{2\Lambda} \iota \sigma^{\mu\nu} (k-p)_\nu + \frac{g_{S^-}}{2\Lambda} (k-p)^\mu \\ & + \frac{g_S}{2\Lambda} (k+p)^\mu + \frac{g_{T^+}}{2\Lambda} \iota \sigma^{\mu\nu} (k+p)_\nu \end{aligned} \quad (2)$$

$$\begin{aligned} \Gamma_A^\mu = & g_A \gamma^\mu \gamma_5 + \frac{f_E}{2\Lambda} \iota \sigma^{\mu\nu} (k-p)_\nu \gamma_5 + \frac{g_{P^-}}{2\Lambda} (k-p)^\mu \gamma_5 \\ & + \frac{g_P}{2\Lambda} (k+p)^\mu \gamma_5 + \frac{g_{T_5^+}}{2\Lambda} \iota \sigma^{\mu\nu} (k+p)_\nu \gamma_5 \end{aligned} \quad (3)$$

Some of the issues concerning the choice of a minimal subset of such couplings are discussed in Ref. [4]. The parameter  $\Lambda_i =$  “the effective-mass scale of new physics”. For  $g_L = 1$  units with  $g_i = 1$ , the nominal size of  $\Lambda_i$  is  $\frac{m_t}{2} = 88 GeV$ , see below. Lorentz equivalence theorems for these couplings are treated in Appendix B. Explicit expressions for the  $A(\lambda_{W^+}, \lambda_b)$  in the case of these additional Lorentz structures are given in Ref. [4].

Improved theoretical treatments of effects of the  $b$  quark mass  $m_b \sim 4.5 GeV$  might also be important because of the small size of the  $b_R$  amplitudes in the SM. In particular, as is discussed below, in many cases if an additional Lorentz structure occurs, finite  $m_b$  effects lead to sizable “oval shapes” as the effective mass scale  $\Lambda_i$  varies. Other recent general analyses of effects in  $t \rightarrow W^+b$  decay associated with new physics arising from large effective-mass scales  $\Lambda_i$  are in Refs. [5-8].

The “arrows” in the upper part of Fig. 1 define the measurable  $\alpha, \beta, \gamma$  relative phases between

the four amplitudes. For instance,

$$\alpha_0 = \phi_0^R - \phi_0^L, \quad \beta_L = \phi_{-1}^L - \phi_0^L, \quad \gamma_+ = \phi_1^R - \phi_0^L \quad (4)$$

where  $A(\lambda_{W^+}, \lambda_b) = |A| \exp(i\phi_{\lambda_{W^+}}^{L,R})$ . So for a pure  $V - A$  coupling, the  $\beta$ 's vanish and all the  $\alpha$ 's and  $\gamma$ 's equal  $+\pi$  (or  $-\pi$ ) to give the intrinsic minus sign of the standard model's  $b_R$  amplitudes.

The lower part of Fig. 1 displays the real part and imaginary part (primed) helicity parameters corresponding to interference measurements of the respective relative phases. For instance, c.f. Appendix C,

$$\begin{aligned} \eta_L &\equiv \frac{1}{\Gamma} |A(-1, -\frac{1}{2})| |A(0, -\frac{1}{2})| \cos \beta_L \\ \eta'_L &\equiv \frac{1}{\Gamma} |A(-1, -\frac{1}{2})| |A(0, -\frac{1}{2})| \sin \beta_L \end{aligned} \quad (5)$$

and

$$\eta_{L,R} = \frac{1}{2}(\eta \pm \omega) \quad (6)$$

Explicit expressions for the eight  $W$ -polarimetry moduli and phase parameters ( $\Gamma, \sigma, \xi, \zeta; \eta, \omega, \eta', \omega'$ ) are given in Ref. [4], along with the inverse formulas for  $\cos(\beta_{L,R}), \sin(\beta_{L,R})$ .

By  $\Lambda_b$  polarimetry[4], or some other  $b$ -polarimetry technique, it might be possible to measure the  $\alpha$  and  $\gamma$  relative phase. In the standard model, the two helicity parameters between the amplitudes with the largest moduli are

$$\begin{aligned} \kappa_0 &\equiv \frac{1}{\Gamma} |A(0, \frac{1}{2})| |A(0, -\frac{1}{2})| \cos \alpha_0 \\ \epsilon_+ &\equiv \frac{1}{\Gamma} |A(1, \frac{1}{2})| |A(0, -\frac{1}{2})| \cos \gamma_+ \end{aligned} \quad (7)$$

We will refer to  $\kappa_0, \epsilon_+$  as the “ $b$ -polarimetry phase parameters”. From Figs. 1 other combinations of relative phases/helicity-parameters are mathematically equivalent.

Unfortunately from the perspective of a complete measurement of the four helicity amplitudes, the tree-level values of  $\kappa_0, \epsilon_+$  in the SM are only about 1%. See the top line in both parts of Table

2, which lists the  $V - A$  values of the helicity parameters for  $m_b = 4.5\text{GeV}$ . In the absence of  $\tilde{T}_{FS}$  violation[4], the relative phases will be interger multiples of  $\pi$  and all prime parameters will vanish. The prime parameters are not directly discussed in this paper.

In Fig. 2 are two probability plots for  $P(W_L) = \frac{1+\sigma}{2}$  versus  $P(b_L) = \frac{1+\xi}{2}$ . The upper plot is for the case of a single additional chiral coupling  $g_i$ . The corners correspond to those of Fig. 1. So the dark rectangle of the SM, gives the relative magnitude of the square of the moduli of its four basic helicity amplitudes. Also, note from the dashed horizontal oval that an additional  $V + A$  coupling does not change the SM expectation that approximately 70% of the final  $W$ 's in  $t \rightarrow W^+b$  decay will be longitudinally polarized.

The endpoints of each oval are at the dark SM rectangle and the dark ellipse where the coupling is pure  $g_i$ . In general, the non-zero area of an oval depends monotonically on  $m_b = 4.5\text{GeV}$  and the area will increase if a larger value is chosen for  $m_b$ . The captions to the figures in this paper discuss the signs of effective-mass scales  $\Lambda_i$  associated with the two parts of each oval which lie between the two endpoints. Appendix A gives numerical values of the  $\Lambda_i$  corresponding to various values of the helicity parameters.

The lower plot in Fig. 2 is for the case of a single additional non-chiral coupling  $V, S, f_M$  ( $A, P, f_E$ ). The corresponding ovals in the two non-chiral plots are almost identical in shape. The  $g_V$  ( $g_A$ ) endpoints lie on the upper(lower) parts of their ovals.

In this paper, we omit the  $A, P, f_E$  curves corresponding to the ones provided for  $V, S, f_M$  because by Lorentz invariance the corresponding ovals, etc., are almost identical. The slight shape differences are very minor to the eye and are definitely negligible versus the resolutions of the forthcoming experiments and the omitted higher order theoretical contributions. The necessary

mirror reflections, in a few cases, to produce the omitted curves are explained in the captions to the figures.

## 2 Moduli Parameters and Phase-Type Ambiguities

Versus predictions based on the SM, two phase-type ambiguities arise by consideration of the effects of a single additional “chiral” coupling  $g_i$  on the three moduli parameters  $\sigma = P(W_L) - P(W_T)$ ,  $\xi = P(b_L) - P(b_R)$ , and  $\zeta = \frac{1}{\Gamma}(\Gamma_L^{b_L - b_R} - \Gamma_T^{b_L - b_R})$ . The partial width  $\Gamma$  for  $t \rightarrow W^+ b$  is the remaining and very important moduli parameter. However, since  $\Gamma$  sets the overall scale, it cannot be well measured by spin-correlation techniques, which better measure the ratios of moduli and relative phases. So, we consider  $\Gamma$  separately; see also [9] and references therein.

For an additional  $S + P$  coupling with  $\Lambda_{S+P} \sim -34.5 GeV$  the values of  $(\sigma, \xi, \zeta)$  and also of the partial width  $\Gamma$  are about the same as the SM prediction, see Table 2. This is the first ambiguity. The dependence of the  $\sigma / P(W_L)$  value versus the effective-mass scale  $\Lambda_{S+P}$  is shown in the upper plot in Fig. 3. Table 1 shows that this ambiguity will also occur if the sign of the  $A_X(0, -\frac{1}{2})$  amplitude for  $g_L + g_X$  is taken to be opposite to that of the SM’s amplitude. Recall that an additional  $S \pm P$  only effects the longitudinal  $W^\pm$  amplitudes and not the transverse  $\lambda_W = \mp 1$  ones. By requiring that

$$\frac{A_X(0, -\frac{1}{2})}{A_X(-1, -\frac{1}{2})} = - \frac{A_L(0, -\frac{1}{2})}{A_L(-1, -\frac{1}{2})} \quad (8)$$

for  $X = S + P$ , we obtain

$$\Lambda_{S+P} = -\left(\frac{g_{S+P}}{g_L}\right) \frac{m_t q_W}{2(E_W + q_W)} \sim -\left(\frac{g_{S+P}}{g_L}\right) \frac{m_t}{4} \left(1 - \left(\frac{m_W}{m_t}\right)^2\right) \quad (9)$$

in the notation of [4].

Several different definitions can be used to characterize the phase-type ambiguities we consider in this section. It is important, we think, to regard these ambiguities from (i) the signs in their  $b_L$  amplitudes versus those for the SM, c.f. Table 1, and from (ii) their associated additional Lorentz structures. From this perspective, the precise characterization of  $\Lambda_{S+P}$ , as in (8,9) for example, is not so important. However, if a non-SM sign were discovered to occur in nature, further analysis and precise measurements would be warranted.

For an additional  $f_M + f_E$  coupling with  $\Lambda_{f_M+f_E} \sim 53\text{GeV}$  the values of  $(\sigma, \xi, \zeta)$  are also about the same as the SM prediction, see Table 2. This is the second ambiguity. In this case, the partial width  $\Gamma$  is about half that of the SM due to destructive interference. The dependence of the  $\sigma / P(W_L)$  value versus the effective-mass scale  $\Lambda_{f_M+f_E}$  is shown in the lower plot of Fig. 3. Table 1 shows that this ambiguity will also occur if the sign of the  $A_X(-1, -\frac{1}{2})$  amplitude for  $g_L + g_X$  is taken to be opposite to that of the SM's amplitude. Again, from (8) for  $X = f_M + f_E$ , we obtain

$$\Lambda_{f_M+f_E} = \left(\frac{g_{f_M+f_E}}{g_L}\right) \frac{m_t E_W}{2(E_W + q_W)} \sim \left(\frac{g_{f_M+f_E}}{g_L}\right) \frac{m_t}{4} \left(1 + \left(\frac{m_W}{m_t}\right)^2\right) \quad (10)$$

from Eqs.(31) in [4] since  $\frac{m_b \sqrt{E_b - q_W}}{m_t \sqrt{E_b + q_W}} \sim 10^{-3}$ .

These phase-type ambiguities are, of course, not the same dynamical issue as finding a combination of  $f_M + f_E$  and  $S + P$  couplings which give the identical  $b_L$  amplitudes as for a pure  $V - A$  coupling. By the expressions in Appendix B, this is possible if  $\Lambda_{S+P} = -\Lambda_{f_M+f_E} = \frac{m_t}{2} \left(1 - \left(\frac{m_b}{m_t}\right)^2\right) = 87\text{GeV}$  and a negligible  $\Lambda_{S-P} = -\Lambda_{f_M-f_E} = -\frac{(m_t)^2}{2m_b} \left(1 - \left(\frac{m_b}{m_t}\right)^2\right) = -3,401\text{GeV}$ . Alternatively, the fundamental  $V$  coupling is removed by  $\Lambda_S = -\Lambda_{f_M} = (m_t + m_b)$  and the  $A$  coupling by  $\Lambda_{f_E} = -\Lambda_P = (m_t - m_b)$ .

Besides the  $f_M + f_E$  construction of this second phase-type ambiguity, it should be kept in mind that some other mechanism might produce the relative sign change shown in Table 1, but

without also changing the absolute value of the  $b_L$  amplitudes. In this case the measurement of the partial width  $\Gamma$  would not resolve the phase ambiguity.

From consideration of Table 1, a third (phase) ambiguity can be constructed by making an arbitrary sign-flip in the  $b_L$  amplitudes, so  $A_X(\lambda_W, \lambda_b = -\frac{1}{2}) = -A_{V-A}(\lambda_W, \lambda_b = -\frac{1}{2})$ , with no corresponding sign changes in the  $b_R$  amplitudes. Resolution of this ambiguity will require  $b$ -polarimetry, c.f. [4], or some other amplitude interference measurement of the overall sign of the  $b_L$  amplitudes relative to the  $b_R$  amplitudes.

In Figs. 4 are plotted the moduli parameters  $\zeta$  versus  $\sigma$  for the case of a single additional coupling  $g_i$ . The figures are for the case of an additional chiral (non-chiral) coupling.

From the perspective of possible additional Lorentz structures, measurement of the partial width  $\Gamma$  is an important constraint. In particular, this provides a strong constraint on possible  $V + A$  couplings, see top part of Fig. 5, in contrast to measurement of  $\sigma / P(W_L)$  which does not, recall Fig. 2. The remaining parts of Fig. 5 are for  $S \pm P$  ( $f_M \pm f_E$ ). Likewise, as shown in the top part of Figs. 6,  $\Gamma$  provides a useful constraint for the possibility of additional  $V$  and  $A$  couplings which are appealing from the perspective of additional gauge-theoretic structures. Here also, the lower part of this figure is for an additional  $S, f_M$  ( $P, f_E$ ) coupling.

### 3 Phase Parameters

In Figs. 7 are plotted the  $\eta$  versus  $\omega$  for the case of a single additional coupling  $g_i$ . The figures are for the case of an additional chiral (non-chiral) coupling. Quite dramatically in the upper plot, the  $S + P$  and  $f_M + f_E$  ambiguities both correspond to a “pseudo-image of the SM rectangle”. This image is in the third quadrant on the diagonal at  $(\eta, \omega) = (-0.46, -0.46)$ . As shown in the

bottom part of Table 2, measurement of the signs of either of the  $W$ -polarimetry phase parameters  $\eta$  or  $\omega$  will resolve both the  $S + P$  and the  $f_M + f_E$  phase-type ambiguities. In the SM, these parameters are sizable and are equal if the  $b_R$  amplitudes are omitted, see eqs.(5,6).

As discussed above, determination of the  $\alpha$  and  $\gamma$  relative phases, as well as resolution of the third ambiguity, will require direct empirical information about the  $b_R$  amplitudes. One way would be from the  $b$ -polarimetry phase parameters  $\epsilon_+$  and  $\kappa_0$ . In Figs. 8 are plotted  $\epsilon_+$  versus  $\eta_L$  for the case of a single additional coupling  $g_i$ . The figures are for the case of an additional non-chiral (chiral) coupling. Here in general, the non-chiral couplings produce larger values for  $\kappa_0$  and  $\epsilon_+$  and so we display the non-chiral case first. In particular, additional  $S + P$  and  $f_M + f_E$  couplings have negligible effects on  $\epsilon_+$  and  $\kappa_0$ , see captions.

Not shown in these figures for  $(\epsilon_+, \eta_L)$  and  $(\kappa_0, \eta_L)$  is the unitarity limit, which is a circle of radius  $\frac{1}{2}$  centered on the origin.

In Figs. 9 are plotted  $\kappa_0$  versus  $\eta_L$  for the case of a single additional coupling  $g_i$ . The figures are for the case of an additional non-chiral (chiral) coupling.

## 4 Ambiguities Among Other Lorentz Structures

From the plots for the various helicity parameters, it is evident that there also are ambiguities within certain subsets of the couplings if an additional Lorentz structure were to occur in the form of a single additional  $g_i$ . The occurrence of an additional Lorentz structure would also raise the issue of how the sign of its  $\Lambda_i$  could be determined.

The following equivalence classes among additional Lorentz structures (versus subsets of possible experimental tests) is another consequence of the underlying Lorentz invariance of (2,3),

etc. Second, with only  $W$ -polarimetry, the effects of the non-zero  $m_b$  mass ( $m_b = 4.5\text{GeV}$ ) are negligible for (i) additional gauge couplings  $V, A, V + A$  and for (ii) additional chiral couplings. However, there is a sizable  $m_b$  dependence in some chiral couplings in the  $(\epsilon_+, \eta_L)$  and  $(\kappa_0, \eta_L)$  plots. In general for additional  $S, P, f_M, f_E$  couplings, the dependence on  $m_b$  is sizable and is likely to be a serious systematic effect, for instance in excluding possible effects from fundamental or induced couplings with these Lorentz structures.

#### 4.1 Additional $V + A, V, \text{ or } A$ couplings

From the gauge theory viewpoint, it is important to search for additional vector and axial vector couplings. The SM's  $P(W_L)$  and  $\eta$  values are only slightly affected by them. But the values for  $\xi$  (equivalently  $P(b_L)$ ),  $\zeta, \omega, \epsilon_+$ , and  $\kappa_0$  are significantly different from those of the SM. However, inspection of the figures shows that in many of the plots the ovals for  $V + A, V, A$  are approximately degenerate. Nevertheless, from the different locations of their endpoints in Figs.(8-9), the  $\epsilon_+, \eta_L, \kappa_0$  parameters could be useful in resolving them. So  $b$ -polarimetry or  $\Gamma$  would generally be useful to resolve these additional couplings and to determine the sign of the associated  $\Lambda_i$ .

#### 4.2 Additional $S - P, S, \text{ or } P$ couplings

For  $S, P$ , versus  $S - P$  there are differences in some of the plots but sufficient resolution and control of possible  $m_b$  effects would be needed. In particular, the narrow  $S - P$  oval and the degenerate fat  $S, P$  ovals lie approximately in the same  $P(W_L), P(b_L)$  regions and also in the same  $\zeta, \sigma$  regions. The sign of  $\Lambda_i$  is the same for the  $S$  and  $P$  ovals. If  $\eta, \omega < 0$ , it would exclude  $S - P$  and would determine the respective sign of  $\Lambda_i$ . The  $\kappa_0, \eta_L$  plot is useful for distinguishing  $S$  versus  $P$  and

for the sign of  $\Lambda_i$ . If  $S - P$  were resolved, then  $\kappa_0$  would give the sign of  $\Lambda_i$ .  $\Gamma$  is not useful for separating  $S$  versus  $P$ , but  $\Gamma$  is different for  $S - P$ .

### 4.3 Additional $f_M + f_E$ or $S + P$ couplings

$f_M + f_E$  and  $S + P$  can be distinguished from either the  $P(W_L), P(b_L)$  or  $\zeta, \sigma$  plots. Once separated,  $\Gamma$  could provide information on the sign of  $\Lambda_i$ . If  $\eta, \omega < 0$ , it would determine the respective sign of  $\Lambda_i$ .  $\epsilon_+ \simeq \kappa_0 \simeq 0$  for these couplings.

### 4.4 Additional $f_M - f_E$ , $f_M$ , or $f_E$ couplings

With sufficient resolution and control of  $m_b$  effects,  $f_M - f_E$  could be separated versus  $f_M, f_E$  by  $P(W_L), P(b_L)$ ; by the  $\zeta, \sigma$  plot; and/or by  $\Gamma$ . The  $\epsilon_+, \eta_L$  plot would be useful for separating  $f_M$  from  $f_E$  and in determining the sign of  $\Lambda_i$ . It would also determine the sign for  $f_M - f_E$ .

## Acknowledgments

One of us(CAN) thanks the Fermilab Theory Group for a useful and intellectually stimulating visit. For computer services, we thank Mark Stephens. This work was partially supported by U.S. Dept. of Energy Contract No. DE-FG 02-96ER40291.

## Appendices

### A Effective-mass scales $\Lambda_i$ corresponding to values of the helicity parameters

The preceding plots do not quantitatively display the effective-mass scales  $\Lambda_i$  associated with the ovals for the respective  $g_{Total} = g_L + g_X$  Lorentz structures. Instead, we present this information in Tables 3-6. Note that  $P(W_L) = \frac{1+\sigma}{2}$  and  $P(b_L) = \frac{1+\xi}{2}$ .

### B Lorentz equivalence theorems

In the case of non-chiral couplings and with the signs and normalizations of (2,3), the tensorial  $f_M$  coupling can be absorbed by using

$$g'_V = g_V - (m_t + m_b) \frac{f_M}{2\Lambda_M}, \quad \frac{g'_S}{2\Lambda'_S} = \frac{g_S}{2\Lambda_S} + \frac{f_M}{2\Lambda_M}, \quad (11)$$

or alternatively, the scalar  $S$  coupling can be absorbed

$$g'_V = g_V + (m_t + m_b) \frac{g_S}{2\Lambda_S}, \quad \frac{f'_M}{2\Lambda'_M} = \frac{f_M}{2\Lambda_M} + \frac{g_S}{2\Lambda_S}. \quad (12)$$

Similarly,  $f_E$  can be absorbed by

$$g'_A = g_A + (m_t - m_b) \frac{f_E}{2\Lambda_E}, \quad \frac{g'_P}{2\Lambda'_P} = \frac{g_P}{2\Lambda_P} + \frac{f_E}{2\Lambda_E}, \quad (13)$$

or alternatively  $P$  by

$$g'_A = g_A - (m_t - m_b) \frac{g_P}{2\Lambda_P}, \quad \frac{f'_E}{2\Lambda'_E} = \frac{f_E}{2\Lambda_E} + \frac{g_P}{2\Lambda_P}. \quad (14)$$

The  $g_{T^+}$  is absorbed by  $g_V \rightarrow g'_V = g_V - (m_t - m_b) \frac{g_{T^+}}{2\Lambda_{T^+}}$  and  $g_{T_5^+}$  by  $g_A \rightarrow g'_A = g_A + (m_t + m_b) \frac{g_{T_5^+}}{2\Lambda_{T_5^+}}$ .

In the case of the chiral combinations, the tensorial  $g_{\pm} \equiv f_M \pm f_E$  are absorbed by using

$$\begin{aligned} g'_L &= g_L - m_t \frac{g_+}{2\Lambda_+} - m_b \frac{g_-}{2\Lambda_-}, & \frac{g'_{S+P}}{2\Lambda'_{S+P}} &= \frac{g_{S+P}}{2\Lambda_{S+P}} + \frac{g_+}{2\Lambda_+}, \\ g'_R &= g_R - m_t \frac{g_-}{2\Lambda_-} - m_b \frac{g_+}{2\Lambda_+}, & \frac{g'_{S-P}}{2\Lambda'_{S-P}} &= \frac{g_{S-P}}{2\Lambda_{S-P}} + \frac{g_-}{2\Lambda_-}, \end{aligned} \quad (15)$$

or alternatively  $S \pm P$  by

$$\begin{aligned} g'_L &= g_L + m_t \frac{g_{S+P}}{2\Lambda_{S+P}} + m_b \frac{g_{S-P}}{2\Lambda_{S-P}}, & \frac{g'_+}{2\Lambda'_+} &= \frac{g_+}{2\Lambda_+} + \frac{g_{S+P}}{2\Lambda_{S+P}}, \\ g'_R &= g_R + m_t \frac{g_{S-P}}{2\Lambda_{S-P}} + m_b \frac{g_{S+P}}{2\Lambda_{S+P}}, & \frac{g'_-}{2\Lambda'_-} &= \frac{g_-}{2\Lambda_-} + \frac{g_{S-P}}{2\Lambda_{S-P}}. \end{aligned} \quad (16)$$

The  $\tilde{g}_{\pm} = g_{T^+} \pm g_{T_5^+}$  are absorbed by  $g_L \rightarrow g'_L = g_L - m_t \frac{\tilde{g}_+}{2\Lambda_+} + m_b \frac{\tilde{g}_-}{2\Lambda_-}$  and  $g_R \rightarrow g'_R = g_R - m_t \frac{\tilde{g}_-}{2\Lambda_-} + m_b \frac{\tilde{g}_+}{2\Lambda_+}$

## C Formulas for $\alpha, \beta, \gamma$ phases from helicity parameters

Eqs.(5,6) define the  $\eta_{L,R}$  helicity parameters associated with the  $\beta_{L,R}$  phases. Similarly, from Figs.

1 the parameters associated with the  $\alpha_{0,1}$  and  $\gamma_{\pm}$  phases are

$$\begin{aligned} \kappa_0 &= \frac{1}{2}(\lambda + \kappa) \equiv \frac{1}{\Gamma} |A(0, -\frac{1}{2})| |A(0, \frac{1}{2})| \cos \alpha_0 \\ \kappa_1 &= \frac{1}{2}(\lambda - \kappa) \equiv \frac{1}{\Gamma} |A(-1, -\frac{1}{2})| |A(1, \frac{1}{2})| \cos \alpha_1 \\ \epsilon_+ &= \frac{1}{2}(\delta + \epsilon) \equiv \frac{1}{\Gamma} |A(1, \frac{1}{2})| |A(0, -\frac{1}{2})| \cos \gamma_+ \\ \epsilon_- &= \frac{1}{2}(\delta - \epsilon) \equiv \frac{1}{\Gamma} |A(-1, -\frac{1}{2})| |A(0, \frac{1}{2})| \cos \gamma_- \end{aligned} \quad (17)$$

The corresponding primed parameters are defined by replacing the cosine by sine.

The inverse formulas for  $\cos \beta_{L,R}$ ,  $\sin \beta_{L,R}$  from  $\eta_{L,R}$  and  $\eta'_{L,R}$  are given by Eqs. (56-59) in [4].

For extracting the  $\alpha_{0,1}$  and  $\gamma_{\pm}$  phases,

$$\begin{aligned}
\cos \alpha_0 &= \frac{4\kappa_0}{\sqrt{(1+\sigma)^2 - (\xi+\zeta)^2}} \\
\cos \alpha_1 &= \frac{4\kappa_1}{\sqrt{(1-\sigma)^2 - (\xi-\zeta)^2}} \\
\cos \gamma_+ &= \frac{4\epsilon_+}{\sqrt{(1+\zeta)^2 - (\sigma+\xi)^2}} \\
\cos \gamma_- &= \frac{4\epsilon_-}{\sqrt{(1-\zeta)^2 - (\sigma-\xi)^2}}
\end{aligned} \tag{18}$$

and the sine's of the respective angles are obtained by using the primed helicity parameter in the respective numerator.

## References

- [1] F. Abe, et. al. (CDF collaboration), Phys. Rev. Lett. **74**, 2626(1995); S. Abachi, et. al. (D0 collaboration), Phys. Rev. Lett. **74**, 2632(1995).
- [2] ATLAS Technical Proposal, CERN/LHCC/94-43, LHCC/P2 (1994); CMS Technical Design Report, CERN-LHCC-97-32; CMS-TDR-3 (1997).
- [3] M. Jezabek and J.H. Kuhn, Phys. Lett. **B207**, 91(1988); **B329**, 317(1994); Nuc. Phys. **B314**, 1(1989); **B320**, 20(1989); C.S. Li, R. Oakes and T.C. Yuan, Phys. Rev. **D43**, 3759(1991); T. Mehen, Phys. Lett. **B417**, 353(1998); A. Czarnecki and K. Melnikov, hep-ph/9806244.
- [4] C.A. Nelson, B.T. Kress, M. Lopes, and T.P. McCauley, Phys. Rev. **D56**, 5928(1997); **D57**, 5923(1998).
- [5] F. Larios, E. Malkawi, C.-P. Yuan, Acta Phys. Polon. **B27**, 3741(1996); hep-ph/9704288; H.-J. He, Y.-P. Kuang, C.-P. Yuan, hep-ph/9704276.

- [6] G.J. Gounaris, F.M. Renard and C. Verzegnassi, Phys. Rev. **D52**, 451(1995); G.J. Gounaris, D.T. Papadamou and F.M. Renard, Z. Phys. **C76**, 333(1997).
- [7] B. Lampe, Phys. Lett. **B415**, 63(1997); B. Grzadkowski, Z. Hioki, M. Szafranski, hep-ph/9712357.
- [8] K. Whisnant, J.M. Yang, B.-L. Young and Z. Zhang, Phys. Rev. **D56**, 467(1997); J.M. Yang and B.-L. Young, *ibid.*, **D56**, 5907(1997); J.-J. Cao, *et.al.*, hep-ph/9804343.
- [9] A.S. Belyaev, E.E. Boos and L.V. Dudkov, hep-ph/9806332; M.C. Smith and S.S. Willenbrock, Phys. Rev. **D54**, 6696(1996); R. Pittau, Phys. Lett. **B386**, 397(1996); A.P. Heinson, A.S. Belyaev and E.E. Boos, hep-ph/9612424.

## Table Captions

Table 1: For the  $(\sigma, \xi, \zeta)$  ambiguous-moduli points, numerical values of the associated helicity amplitudes  $A(\lambda_{W^+}, \lambda_b)$ . The values for the amplitudes are listed first in  $g_L = 1$  units, and second as  $A_{new} = A_{g_L=1}/\sqrt{\Gamma}$  which removes the effect of the differing partial width,  $\Gamma$  for  $t \rightarrow W^+b$ . [ $m_t = 175GeV$ ,  $m_W = 80.35GeV$ ,  $m_b = 4.5GeV$  ].

Table 2: For the  $(\sigma, \xi, \zeta)$  ambiguous-moduli points, numerical values of the associated helicity parameters. Listed first are the four moduli parameters. Listed second are the values of phase parameters which could be used to resolve the ambiguities.

Table 3: Numerical values of the associated helicity parameters  $\sigma, \xi, \zeta, \eta$ , and  $\omega$  as the effective-mass scales  $\Lambda_i$  for additional chiral Lorentz structures vary over the range  $(-5000GeV, 5000GeV)$ . For an additional  $V + A$  coupling,  $g_R$  varies over the range  $(-1.6667, 1.6667)$  with fixed  $g_L = 1$ .

Table 4: Numerical values of the associated helicity parameters  $\sigma, \xi, \zeta, \eta$ , and  $\omega$  as the effective-mass scales  $\Lambda_i$  for additional non-chiral Lorentz structures vary over the range  $(-5000GeV, 5000GeV)$ . For an additional  $V$  or  $A$  coupling,  $g_{V,A}$  respectively varies over the range  $(-1.6667, 1.6667)$  with fixed  $g_L = 1$ .

Table 5: Numerical values of the associated helicity parameters  $\Gamma, \eta_L, \kappa_0$ , and  $\epsilon_+$  as the effective-mass scales  $\Lambda_i$  for additional chiral Lorentz structures vary over the range  $(-5000GeV, 5000GeV)$ . For an additional  $V + A$  coupling,  $g_R$  varies over the range  $(-1.6667, 1.6667)$  with fixed  $g_L = 1$ .

Table 6: Numerical values of the associated helicity parameters  $\Gamma, \eta_L, \kappa_0$ , and  $\epsilon_+$  as the effective-mass scales  $\Lambda_i$  for non-chiral Lorentz structures vary over the range  $(-5000GeV, 5000GeV)$ . For an additional  $V$  or  $A$  coupling,  $g_{V,A}$  respectively varies over the range  $(-1.6667, 1.6667)$  with fixed  $g_L = 1$ .

## Figure Captions

FIG. 1: For  $t \rightarrow W^+b$  decay, display of the four helicity amplitudes  $A(\lambda_{W^+}, \lambda_b)$  relative to the  $b$  quark's helicity. The upper sketch defines the measurable “ $\alpha, \beta, \gamma$ ” relative phases, c.f. Eqs(4). The lower sketch defines the real part and imaginary part (primed) helicity parameters corresponding to these relative phases.

FIG. 2: For the case of a single additional coupling ( $g_i$ ), plots of the probability,  $P(W_L)$ , that the emitted  $W^+$  is “Longitudinally” polarized versus the probability,  $P(b_L)$ , that the emitted  $b$ -quark has “Left-handed” helicity. The upper plot is for additional chiral couplings: a dark rectangle denotes the value for the pure  $V - A$  coupling of the standard model. The long-dashed (horizontal) oval is for an additional  $V + A$  coupling. A dark ellipse denotes the end point where the coupling is pure  $V + A$ , and similarly for the other ovals. The dashed oval is for an additional  $f_M - f_E$  coupling. The dashed-dot oval is for an addition  $S - P$  coupling. The solid (zero-area) vertical ovals with  $P(b_L) = 1$  which end above/below the  $V - A$  point are for an additional  $f_M + f_E$  /  $S + P$  coupling. The upper(lower) portions of the ovals are for  $\Lambda_i > 0 (< 0)$ , except for the solid curves  $f_M + f_E$  and  $S + P$  which cover the full  $P(W_L)$  range for small  $\Lambda_i$  values, see the  $P(W_L)$  versus  $\Lambda_i$  plots in Figs. 3. The lower plot is for additional non-chiral coupling  $V, S, f_M$  couplings. The long-dashed (horizontal) oval is for an additional  $V(A)$  coupling. The dashed oval is for an additional  $f_M(f_E)$  coupling. The dashed-dot oval is for an addition  $S(P)$  coupling.  $\Lambda_i > 0$  corresponds to the tops of the ovals from the  $V - A$  solid rectangle to the pure  $g_i$  endpoints. To the eye, the omitted (see Sec. 1) respective curves for  $A, P, f_E$  almost overlap the ones for  $V, S, f_M$ . For  $A$ , the endpoint is slightly below (that for  $V$ ) and on the bottom arc of its oval.

FIG. 3: The upper(lower) plot displays the  $P(W_L)$  value versus the effective-mass scale  $\Lambda$  for

an additional  $S + P$  ( $f_M + f_E$ ) coupling. The ambiguous- moduli point for this coupling occurs at  $\Lambda_{S+P} \sim -34.5 GeV$  ( $\Lambda_{f_M+f_E} \sim 52.9 GeV$ ) where the solid curve crosses over the dashed horizontal line which shows the standard V-A value.

FIG. 4: For the case of a single additional coupling ( $g_i$ ), plots of the moduli parameters  $\zeta$  versus  $\sigma$ . The ovals are labeled as in Fig. 2.  $\Lambda_i > 0$  corresponds to the right-sides of the ovals from the  $V - A$  rectangle to the pure  $g_i$  endpoints. In the upper plot for additional chiral couplings, the  $S + P$  ( $f_M + f_E$ ) endpoint is in the first(third) quadrant. The lower plot is for additional  $V, S, f_M$  couplings. To the eye, the omitted respective curves for  $A, P, f_E$  almost overlap. The  $A$  endpoint is slightly to the left, on the origin side of the oval.

FIG. 5: Plots of the partial width for  $t \rightarrow W^+b$  versus strengths of an additional chiral coupling: upper-figure is for an additional  $V + A$  coupling; middle- figure's solid ( dashed-dot) curve is for  $S + P$  ( $S - P$ ); and lower-figure's solid ( dashed-dot) curve is for  $f_M + f_E$  ( $f_M - f_E$ ).

FIG. 6: Plots of the partial width for  $t \rightarrow W^+b$  versus strengths of an additional non-chiral coupling  $V, S, f_M$ : upper-figure is for an additional  $V$  coupling; and lower- figure's dashed-dot ( dotted ) curve is for  $S$  ( $f_M$ ). The omitted plot for  $A$  is almost the mirror image about the  $\Gamma$  axis of  $V$ 's, so  $\Gamma(g_A) \approx \Gamma(-g_V)$ . Those for  $P, f_E$  are respectively about the same as for  $S, f_M$ .

FIG. 7: Plots of the two W-polarimetry phase parameters,  $\eta, \omega$  for the case of a single additional coupling ( $g_i$ ). The ovals are labeled as in Fig. 2.  $\Lambda_i > 0$  correspond to the lower parts of the ovals from the  $V - A$  rectangle to the pure  $g_i$  endpoints. The upper plot is for additional chiral couplings and the first two phase-type ambiguities correspond to a “pseudo-image of the SM rectangle” at  $(-0.46, -0.46)$ . The  $S \pm P$  end points are at the origin. On the solid line (zero area) ovals, the  $f_M + f_E$  end point is in the first quadrant, and both the  $f_M + f_E$  and  $S + P$  ovals extend through

the third quadrant with respectively  $\Lambda_i > 0, < 0$ . The  $f_M + f_E$  and  $S + P$  ovals each cover the entire diagonal. The lower plot is for additional  $V, S, f_M$  ( $A, P, f_E$ ) couplings. On the vertical axis, the  $V(A)$  end point is at the bottom(top) of its horizontal oval. Similarly, near the origin the  $S(P)$  end point is at the bottom(top) of its oval.

FIG. 8: Plots of the b-polarimetry phase parameter  $\epsilon_+$  versus  $\eta_L$  for the case of a single additional coupling ( $g_i$ ). The upper plot is for additional  $V, S, f_M$  couplings.  $\Lambda_i > 0$  corresponds to the upper part of the long-dashed  $V$  oval from the  $V - A$  rectangle, the lower part of the dotted  $f_M$ , and the positive  $\eta_L$  part of the dashed-dot  $S$ . The latter, zero-area  $S$  oval extends to  $\eta_L \sim -1.2$ . The omitted  $A, P, f_E$  plot is almost the mirror image about the  $\eta_L$  axis, in it  $\Lambda_i > 0$  corresponds to the upper parts of the long-dashed  $A$  and dotted  $f_E$  ovals from the  $V - A$  rectangle, and the positive  $\eta_L$  part of the dashed-dot  $P$ . The lower plot is for a single additional chiral coupling. Only the  $f_M + f_E$  endpoint is not near the origin. The  $\epsilon_+$  values are non-negligible for only two couplings:  $\Lambda_i > 0$  corresponds to the upper part of the long-dashed  $V + A$  oval from the  $V - A$  rectangle, the lower part of the dotted  $f_M - f_E$  oval. For the other couplings, their  $\eta_L = \eta + \omega$  dependence is shown in Fig. 7.

FIG. 9: Plots of the b-polarimetry phase parameter  $\kappa_0$  versus  $\eta_L$  for the case of a single additional ( $g_i$ ). The upper plot is for additional  $V, S, f_M$  couplings.  $\Lambda_i > 0$  corresponds to the upper part of the long-dashed  $V$  and the dashed-dot  $S$  ovals from the  $V - A$  rectangle, and corresponds to the lower part of the dotted  $f_M$ . The omitted  $A, P, f_E$  plot is almost the mirror image about the  $\eta_L$  axis. In it,  $\Lambda_i > 0$  corresponds to the upper parts of the long-dashed  $A$  and dotted  $f_E$  ovals from the  $V - A$  rectangle, and corresponds to the lower part part of the dashed-dot  $P$ . The lower plot is for a single additional chiral coupling. Only the  $f_M + f_E$  endpoint is not

near the origin. The  $\kappa_0$  values are non-negligible for three couplings:  $\Lambda_i > 0$  corresponds to the upper part of the long-dashed  $V + A$  and dashed-dot  $S - P$  ovals from the  $V - A$  rectangle, and corresponds to the lower part of the dotted  $f_M - f_E$  oval.

Table 1: Amplitudes at  $(\sigma, \xi, \zeta)$  Ambiguous Points

	$A(0, -\frac{1}{2})$	$A(-1, -\frac{1}{2})$	$A(0, \frac{1}{2})$	$A(1, \frac{1}{2})$
$A_{g_L=1}$ in $g_L = 1$ units				
$V - A$	338	220	-2.33	-7.16
$S + P$	-338	220	-24.4	-7.16
$f_M + f_E$	220	-143	1.52	-4.67
$A_{New} = A_{g_L=1}/\sqrt{\Gamma}$				
$V - A$	0.84	0.54	-0.0058	-0.018
$S + P$	-0.84	0.54	-0.060	-0.018
$f_M + f_E$	0.84	-0.54	0.0058	-0.018

Table 2:  $(\sigma, \xi, \zeta)$  Ambiguous Points

	$\sigma$	$\xi$	$\zeta$	$\Gamma[GeV]$	
$V - A$	0.41	1.00	0.41	1.55GeV	
$S + P$	0.41	0.99	0.40	1.55GeV	
$f_M + f_E$	0.41	1.00	0.41	0.66GeV	
	$\eta$	$\omega$	$\eta_L$	$\kappa_o$	$\epsilon_+$
$V - A$	0.46	0.46	0.46	-0.005	-0.015
$S + P$	-0.45	-0.46	-0.46	-0.05	0.015
$f_M + f_E$	-0.46	-0.46	-0.46	0.005	-0.015

Table 3:  $\sigma, \dots, \omega$  versus effective-mass scales  $\Lambda_i$  for additional chiral Lorentz structures

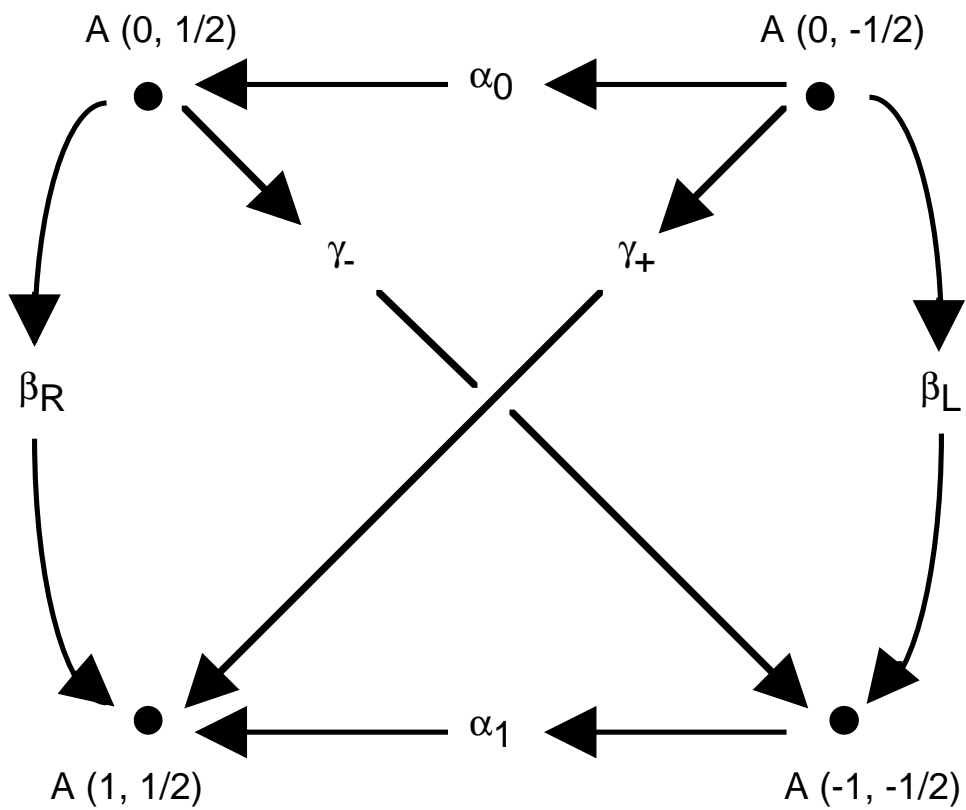
$\Lambda_i$ [GeV] or $g_R$	$\sigma$	$\xi$	$\zeta$	$\eta$	$\omega$
Pure $V - A$	0.4057	0.9993	0.4063	0.4568	0.4566
Additional $V + A$					
-1.6667	0.3873	-0.4585	-0.1864	0.4610	-0.2095
-0.4167	0.3908	0.6894	0.2803	0.4602	0.3150
-0.1667	0.3988	0.9365	0.3807	0.4584	0.4279
-0.0167	0.4050	0.9978	0.4057	0.4570	0.4559
0.0167	0.4064	0.9997	0.4064	0.4567	0.4568
0.1667	0.4127	0.9543	0.3880	0.4553	0.4361
0.4167	0.4213	0.7185	0.2921	0.4534	0.3283
1.6667	0.4251	-0.4826	-0.1962	0.4525	-0.2205
Additional $S + P$					
-5000	0.3940	0.9993	0.3946	0.4594	0.4592
-500	0.2747	0.9990	0.2753	0.4807	0.4803
-200	0.0075	0.9982	0.0078	0.5000	0.4991
-50	-0.4829	0.9890	-0.4907	-0.4317	-0.4355
50	0.8612	0.9994	0.8608	0.2539	0.2541
200	0.6212	0.9996	0.6216	0.3916	0.3917
500	0.5078	0.9995	0.5083	0.4305	0.4305
5000	0.4171	0.9993	0.4177	0.4543	0.4541
Additional $S - P$					
-5000	0.4055	0.9988	0.4055	0.4570	0.4564
-500	0.4107	0.9701	0.3820	0.4530	0.4488
-200	0.4453	0.8368	0.2833	0.4264	0.4167
-50	0.7406	-0.1812	-0.4401	0.1994	0.1814
50	0.7514	-0.1096	-0.3577	0.1911	0.2082
200	0.4579	0.8527	0.3118	0.4167	0.4259
500	0.4165	0.9756	0.3933	0.4486	0.4524
5000	0.4061	0.9993	0.4067	0.4566	0.4568
Additional $f_M + f_E$					
-5000	0.3943	0.9993	0.3948	0.4594	0.4591
-500	0.2965	0.9993	0.2970	0.4774	0.4772
-200	0.1551	0.9994	0.1555	0.4939	0.4937
-50	-0.2598	0.9995	-0.2596	0.4828	0.4826
50	0.2538	0.9994	0.2543	-0.4835	-0.4833
200	0.7199	0.9992	0.7207	0.3466	0.3465
500	0.5262	0.9993	0.5268	0.4250	0.4248
5000	0.4173	0.9993	0.4179	0.4542	0.4540
Additional $f_M - f_E$					
-5000	0.4061	0.9999	0.4062	0.4569	0.4568
-500	0.3981	0.9868	0.4088	0.4558	0.4519
-200	0.3438	0.8974	0.4268	0.4485	0.4184
-50	-0.1985	0.0049	0.6066	0.3758	0.0833
50	-0.2065	-0.0083	0.6093	0.3747	0.0784
200	0.3245	0.8657	0.4332	0.4460	0.4065
500	0.3893	0.9722	0.4117	0.4546	0.4465
5000	0.4051	0.9984	0.4065	0.4568	0.4563

Table 4:  $\sigma, \dots, \omega$  versus effective-mass scales  $\Lambda_i$  for additional non-chiral Lorentz structures

$\Lambda_i$ [GeV] or $g_{V,A}$	$\sigma$	$\xi$	$\zeta$	$\eta$	$\omega$
Pure $V - A$	0.4057	0.9993	0.4063	0.4568	0.4566
Additional $V$					
-1.6667	0.4208	-0.7384	-0.3002	0.4535	-0.3374
-0.4167	0.3860	0.3154	0.1282	0.4612	0.1441
-0.1667	0.3976	0.9123	0.3709	0.4587	0.4169
-0.0167	0.4050	0.9977	0.4056	0.4570	0.4559
0.0167	0.4064	0.9997	0.4065	0.4567	0.4568
0.1667	0.4118	0.9672	0.3932	0.4555	0.4420
0.4167	0.4175	0.8536	0.3470	0.4542	0.3901
1.6667	0.4255	0.4496	0.1828	0.4524	0.2055
Additional $A$					
-1.6667	0.3869	0.4268	0.1735	0.4610	0.1950
-0.4167	0.3943	0.8272	0.3363	0.4594	0.3780
-0.1667	0.3998	0.9516	0.3869	0.4582	0.4348
-0.0167	0.4050	0.9978	0.4057	0.4570	0.4560
0.0167	0.4064	0.9997	0.4064	0.4567	0.4568
0.1667	0.4141	0.9328	0.3793	0.4550	0.4263
0.4167	0.4266	0.3332	0.1355	0.4522	0.1523
1.6667	0.3912	-0.7094	-0.2884	0.4601	-0.3242
Additional $S$					
-5000	0.3938	0.9987	0.3938	0.4596	0.4589
-500	0.2836	0.9614	0.2466	0.4748	0.4694
-200	0.1274	0.7267	-0.1440	0.4396	0.4237
-50	0.6816	-0.5456	-0.8633	-0.0927	-0.1155
50	0.8983	0.5160	0.4146	0.1859	0.1931
200	0.6454	0.8972	0.5434	0.3665	0.3727
500	0.5159	0.9784	0.4953	0.4235	0.4268
5000	0.4175	0.9993	0.4180	0.4540	0.4542
Additional $P$					
-5000	0.3944	0.9993	0.3950	0.4591	0.4593
-500	0.2892	0.9723	0.2630	0.4711	0.4756
-200	0.1314	0.7794	-0.0874	0.4376	0.4518
-50	0.6324	-0.5350	-0.9018	-0.1070	-0.0825
50	0.8899	0.5306	0.4207	0.2013	0.1939
200	0.6352	0.8994	0.5354	0.3771	0.3708
500	0.5105	0.9766	0.4882	0.4282	0.4247
5000	0.4169	0.9988	0.4169	0.4544	0.4539
Additional $f_M$					
-5000	0.3946	0.9998	0.3947	0.4594	0.4594
-500	0.2906	0.9889	0.2997	0.4764	0.4732
-200	0.1205	0.9297	0.1780	0.4867	0.4665
-50	-0.3815	0.5754	-0.0342	0.4409	0.3188
50	-0.4794	-0.3873	0.6550	0.0529	-0.3464
200	0.5736	0.8100	0.7289	0.3416	0.2868
500	0.5051	0.9680	0.5312	0.4229	0.4137
5000	0.4167	0.9983	0.4180	0.4542	0.4537
Additional $f_E$					
-5000	0.3937	0.9984	0.3950	0.4593	0.4588
-500	0.2837	0.9757	0.3031	0.4753	0.4680
-200	0.1100	0.9039	0.1870	0.4845	0.4557
-50	-0.3795	0.5453	-0.0156	0.4416	0.3053
50	-0.4843	-0.3816	0.6209	0.0565	-0.3580
200	0.6063	0.8484	0.7275	0.3427	0.2972
500	0.5164	0.9842	0.5290	0.4240	0.4192
5000	0.4176	0.9999	0.4177	0.4543	0.4542

Table 5:  $\Gamma, \eta_L, \kappa_o, \epsilon_+$  versus effective-mass scales  $\Lambda_i$  for additional chiral Lorentz structures

$\Lambda_i$ [GeV] or $g_R$	$\Gamma$ [GeV]	$\eta_L$	$\kappa_o$	$\epsilon_+$
Pure $V - A$	1.5536	0.4567	-0.0048	-0.0149
Additional $V + A$				
-1.6667	6.0193	0.1257	-0.3071	-0.2026
-0.4167	1.8609	0.3876	-0.2492	-0.1718
-0.1667	1.6118	0.4432	-0.1177	-0.0878
-0.0167	1.5555	0.4565	-0.0165	-0.0225
0.0167	1.5525	0.4568	0.0069	-0.0073
0.1667	1.5817	0.4457	0.1102	0.0601
0.4167	1.7857	0.3908	0.2498	0.1522
1.6667	5.7188	0.1160	0.3133	0.2004
Additional $S + P$				
-5000	1.5236	0.4593	-0.0052	-0.0150
-500	1.2730	0.4805	-0.0084	-0.0157
-200	0.9303	0.4995	-0.0139	-0.0163
-50	0.6226	-0.4336	0.0346	0.0141
50	6.6505	0.2540	0.0149	-0.0083
200	2.4372	0.3916	0.0026	-0.0128
500	1.8758	0.4305	-0.0016	-0.0140
5000	1.5839	0.4542	-0.0045	-0.0148
Additional $S - P$				
-5000	1.5530	0.4567	-0.0145	-0.0149
-500	1.5667	0.4509	-0.1006	-0.0147
-200	1.6644	0.4215	-0.2283	-0.0137
-50	3.5591	0.1904	-0.4065	-0.0062
50	3.7141	0.1996	0.4220	-0.0065
200	1.7031	0.4213	0.2193	-0.0137
500	1.5822	0.4505	0.0909	-0.0147
5000	1.5546	0.4567	0.0049	-0.0149
Additional $f_M + f_E$				
-5000	1.5779	0.4592	-0.0049	-0.0148
-500	1.8111	0.4773	-0.0051	-0.0137
-200	2.2559	0.4938	-0.0052	-0.0122
-50	5.5320	0.4827	-0.0051	-0.0078
50	0.6930	-0.4834	0.0051	-0.0133
200	1.0461	0.3465	-0.0037	-0.0182
500	1.3272	0.4249	-0.0045	-0.0162
5000	1.5295	0.4541	-0.0048	-0.0150
Additional $f_M - f_E$				
-5000	1.5528	0.4569	-0.0022	-0.0069
-500	1.5596	0.4539	0.0210	0.0646
-200	1.6271	0.4335	0.0572	0.1759
-50	3.0171	0.2296	0.1296	0.3987
50	3.2080	0.2265	-0.1296	-0.3987
200	1.6749	0.4262	-0.0649	-0.1996
500	1.5787	0.4506	-0.0303	-0.0934
5000	1.5547	0.4565	-0.0074	-0.0229



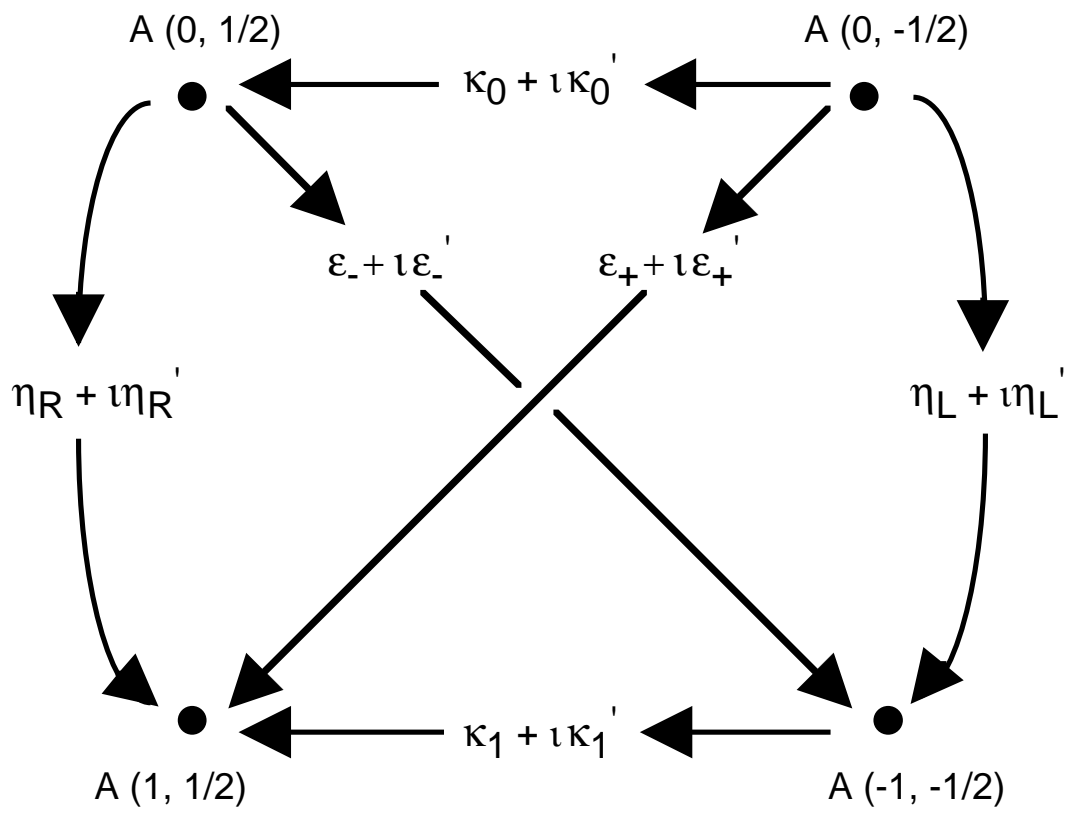
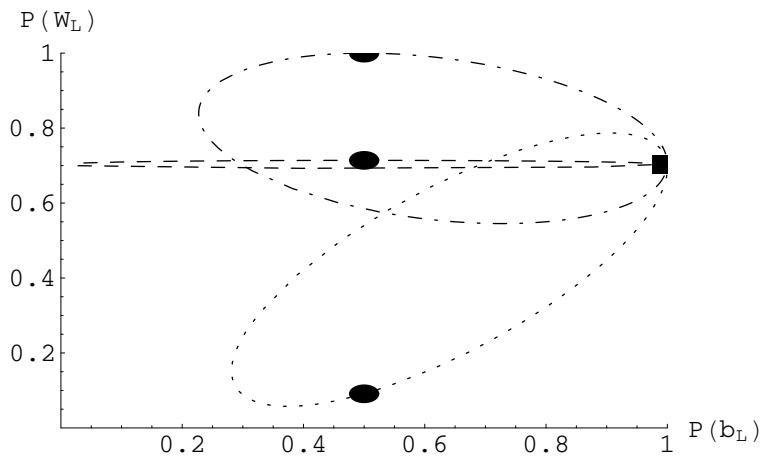
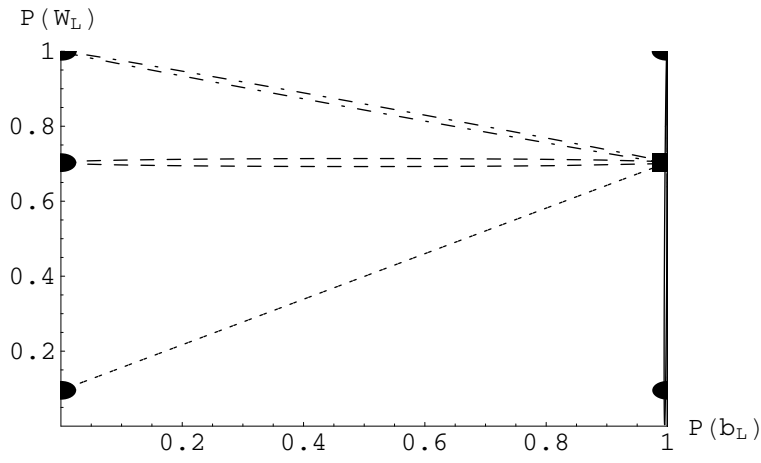


Table 6:  $\Gamma, \eta_L, \kappa_o, \epsilon_+$  versus effective-mass scales  $\Lambda_i$  for additional non-chiral Lorentz structures

$\Lambda_i$ [GeV] or $g_{V,A}$	$\Gamma$ [GeV]	$\eta_L$	$\kappa_o$	$\epsilon_+$
Pure $V - A$	1.5536	0.4567	-0.0048	-0.0149
Additional $V$				
-1.6667	4.9058	0.0580	0.2424	0.1559
-0.4167	0.8203	0.3027	-0.3283	-0.2209
-0.1667	1.1345	0.4378	-0.1385	-0.1012
-0.0167	1.5041	0.4565	-0.0167	-0.0226
0.0167	1.6047	0.4568	0.0067	-0.0074
0.1667	2.1402	0.4487	0.0943	0.0497
0.4167	3.3344	0.4221	0.1884	0.1115
1.6667	14.9623	0.3290	0.3194	0.1989
Additional $A$				
-1.6667	15.7639	0.3280	-0.3126	-0.2114
-0.4167	3.4409	0.4187	-0.1921	-0.1355
-0.1667	2.1753	0.4465	-0.1024	-0.0780
-0.0167	1.6078	0.4565	-0.0163	-0.0223
0.0167	1.5012	0.4568	0.0071	-0.0071
0.1667	1.1095	0.4406	0.1318	0.0743
0.4167	0.7764	0.3022	0.3368	0.2109
1.6667	5.1062	0.0679	-0.2424	-0.1591
Additional $S$				
-5000	1.5231	0.4592	-0.0149	-0.0150
-500	1.2888	0.4721	-0.1086	-0.0154
-200	1.0580	0.4317	-0.2413	-0.0141
-50	2.8994	-0.1041	0.2295	0.0034
50	9.0823	0.1895	0.4136	-0.0062
200	2.6038	0.3696	0.1988	-0.0120
500	1.9071	0.4251	0.0887	-0.0139
5000	1.5849	0.4541	0.0052	-0.0148
Additional $P$				
-5000	1.5246	0.4592	0.0046	-0.0150
-500	1.2989	0.4734	0.0923	-0.0154
-200	1.0629	0.4447	0.2238	-0.0145
-50	2.5119	-0.0948	-0.1937	0.0031
50	8.3848	0.1976	-0.4083	-0.0064
200	2.5311	0.3739	-0.1961	-0.0122
500	1.8862	0.4264	-0.0922	-0.0139
5000	1.5833	0.4541	-0.0141	-0.0148
Additional $f_M$				
-5000	1.5771	0.4594	-0.0023	-0.0069
-500	1.8166	0.4748	0.0180	0.0571
-200	2.3258	0.4766	0.0421	0.1334
-50	6.9373	0.3799	0.0748	0.2365
50	2.2893	-0.1467	-0.1116	-0.3525
200	1.1638	0.3142	-0.0822	-0.2592
500	1.3518	0.4183	-0.0332	-0.1044
5000	1.5306	0.4539	-0.0074	-0.0231
Additional $f_E$				
-5000	1.5790	0.4590	-0.0074	-0.0226
-500	1.8368	0.4716	-0.0278	-0.0837
-200	2.3808	0.4701	-0.0513	-0.1543
-50	7.2447	0.3735	-0.0808	-0.2426
50	2.2147	-0.1508	0.1142	0.3426
200	1.1233	0.3199	0.0778	0.2329
500	1.3338	0.4216	0.0246	0.0734
5000	1.5287	0.4543	-0.0022	-0.0069



This figure "Fig3.gif" is available in "gif" format from:

<http://arxiv.org/ps/hep-ph/9806373v1>

This figure "Fig4.gif" is available in "gif" format from:

<http://arxiv.org/ps/hep-ph/9806373v1>

This figure "Fig5.gif" is available in "gif" format from:

<http://arxiv.org/ps/hep-ph/9806373v1>

This figure "Fig6.gif" is available in "gif" format from:

<http://arxiv.org/ps/hep-ph/9806373v1>

This figure "Fig7.gif" is available in "gif" format from:

<http://arxiv.org/ps/hep-ph/9806373v1>

This figure "Fig8.gif" is available in "gif" format from:

<http://arxiv.org/ps/hep-ph/9806373v1>

This figure "Fig9.gif" is available in "gif" format from:

<http://arxiv.org/ps/hep-ph/9806373v1>